Applied Surface Science 665 (2024) 160290

Contents lists available at ScienceDirect

Applied Surface Science

journal homepage: www.elsevier.com/locate/apsusc

Full Length Article

Designing advanced high-Cr ferrous alloys for next-generation energy applications through cryogenic processing

Patricia Jovičević-Klug [a,b,*], Carsten Bonnekoh [c], Matic Jovičević-Klug [a], Bojan Ambrožič [d], Goran Dražić [e], Zygmunt Miłosz [f], Yan Ma [a], Ingrid McCarroll [a], Benjamin Breitbach [a], Matteo Amati [f], Luca Gregoratti [f], Michael Rieth [f], Michael Rohwerder [a]

[a] Max Planck Institute for Sustainable Materials (Max-Planck-Institut für Eisenforschung GmbH), Max-Planck-Straße 1, 40237 Düsseldorf, Germany
[b] Alexander von Humboldt PostDoc Research Fellow, Alexander von Humboldt Foundation, Jean-Paul-Straße 12, 53173 Bonn, Germany
[c] Institute for Applied Materials, Karlsruhe Institute of Technology, Hermann-von-Helmholtz-Platz 1, 76344 Eggenstein-Leopoldshafen, Germany
[d] Nanocenter, Jamova 39, 1000 Ljubljana, Slovenia
[e] National Institute of Chemistry, Hajdrihova ulica 19, 1000 Ljubljana, Slovenia
[f] Elettra - Sincrotone Trieste, S.C.p.A., SS14 – km 163.5 in Area Science Park, 34149 Trieste, Italy

ARTICLE INFO

Keywords:
High-Cr ferrous alloy (Eurofer)
Cryogenic processing (CP)
Microstructure
Precipitation
Carbides
Oxidation state

ABSTRACT

Excellent properties (durability, wear and corrosion resistance) and long service life under extreme conditions are essential for the successful application of metallic materials in the energy sector. In particular, for future fusion applications, high Cr ferrous alloys (in our case Eurofer) are of great interest. Importantly, modified microstructure with higher dimensional stability improves corrosion and wear resistance properties. In this study, we successfully manipulate the desired type of microstructure, which could provide a solution to current challenges in such a high temperature, highly corrosive and highly irradiated environment, using a novel technique of cryogenic processing (CP). The research identifies the CP-driven changes not only to the microstructure, but also to the local chemistry and bonding state of the key alloying elements. The correlations and individual phenomena associated with CP have been evaluated using state-of-the-art techniques such as atom probe tomography and synchrotron-based in-situ scanning photoemission spectroscopy. This novel process and its novel microstructural manipulation opens up new possibilities for materials processing for future energy applications.

1. Introduction

Improving the microstructure is a critical criterion for materials used in various applications in the energy sector (including fusion sector), as it tailors the final properties such as corrosion resistance, fatigue resistance, and wear resistance as well as magnetism, mechanical properties, and surface properties [1]. Failure of materials in the energy sector can cost up to 1/3 of the investment [2]. It can lead to power plant shutdowns or even disasters, which are directly correlated to microstructural changes and subsequent changes in final properties due to material degradation or alteration under operating conditions [3]. High temperatures and pressures, highly corrosive environments and high-energy particles can be commonly found in future fusion energy applications. Such extreme environments can cause considerable changes in the microstructure of exposed material, an issue that has remained unanswered [4,5]. In addition, strong magnetic fields, helium embrittlement and diffusion as well as thermal fatigue are expected in fusion environment [6], further increasing the risks of progressive material degradation and failure. For construction of the first wall of future fusion reactors as well as in the next-generation fission reactors [5,7], high-Cr reduced activation ferritic-martensitic (RAFM) alloys, such as Eurofer, are considered as the main candidates. Investigations of such materials revealed microstructural changes such as induced alloy segregation, void growth and increased precipitation that form during and after their operation, which ultimately affect the material's properties [8]. The phase changes were mainly related to Cr mobility within the material at local areas such as grain boundaries (GBs) that act as sinks or enrichment zones [9]. The prior austenitic grain boundaries (PAGs) also

* Corresponding author at: Max Planck Institute for Sustainable Materials (Max-Planck-Institut für Eisenforschung GmbH), Max-Planck-Straße 1, 40237 Düsseldorf, Germany.
E-mail address: p.jovicevic-klug@mpie.de (P. Jovičević-Klug).

https://doi.org/10.1016/j.apsusc.2024.160290
Received 12 March 2024; Received in revised form 28 April 2024; Accepted 13 May 2024
Available online 16 May 2024

displayed an increase in Cr concentration, which can modify the final properties of the material due to matrix dealloying and grain boundary (GB) embrittlement [10]. Increased precipitation was associated with the formation of $M_{23}C_6$ carbides, which are considered instable with long exposure times in fusion reactor environments. Additionally, these precipitates displayed agglomeration and coarsening, which can negatively impact the final mechanical properties through embrittlement and swelling. On the other hand, the increased $M_{23}C_6$ precipitation can be also considered favourable since it hardens the material, which can compensate the swelling effect [6]. In addition, the changes in dimensional stability and microstructure cause mismatch between the different phases, resulting in residual stresses within the alloys [11], which are precursors for fracturing of the material from micro-to macro level [11]. These findings not only raise questions about how to deal with these issues, but also provide opportunities for the materials research community to find new ways for modification/tailoring of the microstructure, residual stress state and final properties (fatigue, wear, mechanical properties, etc.) through different techniques or processes. Cryogenic processing (CP) offers a novel way of tailoring the microstructure and properties of materials by exposing them to cryogenic temperatures (typically 77 K) [2]. CP has proven to be an effective solution for improving the properties of stainless and martensitic steels, such as corrosion, oxidation and fatigue resistance as well as improving ductility and strength, therefore extending the life cycle of the treated material or component [2]. Combined with various techniques, namely in-situ observations of alloying dynamics and detailed microstructural analysis of the Eurofer, this work explores and provides novel insight into the processing of Eurofer as well as similar alloys used in the energy sector, including fusion. With the use of cryogenic processing, this study provides a possible answer to reducing CO_2 emissions from the energy sector, steel and tool industries and using more environmentally friendly techniques/processing of various materials, while providing novel combinations of microstructure and properties that provide further stability to alloys under extreme conditions.

2. Methods and materials

2.1. Material, Processing, microstructure and phase analysis

Selected Eurofer alloy is high-Cr ferrous alloy (chemical composition in wt.%: 0.11C, 0.4 Mn, 9 Cr, 0.12 Ta, 1.1 W, 0.03 N, 0.15 V, base Fe, others < 0.01 [12]), also known as Eurofer in fusion community, which was supplied by Karlsruhe Institute of Technology (KIT), Germany. Eurofer samples were divided into two subgroups C-EF and CRYO (T-EF and ST-EF), for details about heat processing, see Table 1, samples were heat treated at Max Planck Institute for Sustainable Materials (new name) (MPI SusMat)/Max-Planck-Institute für Eisenforschung GmbH (old name), Germany. Both subgroups were heat processed in Ar atmosphere under high vacuum, in order to exclude influence of N_2 gas during hardening on the microstructure. CP was done with gradual immersion for 24 h at 77 K, with cooling and warming rate of 10 K/s, which is the standard and recommended rate in order to avoid microcracking of the material [13]. The metallographic preparation of tested samples for further analysis was according to Jovičević-Klug et al. 2021 [13] for ferrous alloys.

Table 1
Heat processing of different subgroups.

Sample group	Heat processing		
	Hardening	CP	Tempering
EF-CHT	Ta = 1237 K/ 0.5 h, Q rate ~ 10 s from 1073 K to 773 K	–	Tt = 823 K / 2 h
CRYO (T-EF, ST-EF)	Ta = 1237 K/ 0.5 h Q rate ~ 10 s from 1073 K to 773 K	DCT 24 h / 77 K	Tt = 823 K / 2 h

Microstructural analysis of Eurofer alloy was performed using a scanning electron microscope (SEM) Zeiss Crossbeam 550 FIB-SEM Merlin II at MPI SusMat, Germany.

For the quantitative phase analysis XRD scans were carried out using a Rigaku SmartLab diffractometer having a Cu Kα rotating anode X-ray source. The diffractometer is equipped with a micro area beam optic (500 μm by 500 μm beam size), a 5-circle goniometer, and a HyPix3000 area detector. The measurements were done as a continuous symmetrical overview scan using a step size of $\Delta 2\Theta = 0.01^{\circ}$, a count rate of 4 deg/min, and a power setup of 45 kV/200 mA. With the measured data the quantification of the single phases calculated using Rietveld simulation (Software Bruker TOPAS V5.0).

2.2. FIB/(S)TEM

Lamellas for the (S)TEM investigations were prepared using Focused Ion Beam (FIB)-SEM dual system (Helios NanoLab 650, FEI, USA) using an in-situ lift-out technique. During the lamella preparation samples were protected with 300 nm thick electron deposited W capping layer and an additional 2.5 μm thick ion deposited capping W layer, which were deposited on top of each other at the selected ion acceleration voltages/beam currents of 20 kV/1.6 nA and 30 kV/0.7 nA, respectively. The sample was extracted with gallium ions at 30 kV/21 nA. In the next step samples were transferred with an OmniProbe 200 micromanipulator on the Cu FIB lift out grids where final thinning and polishing of lamella was performed: using accelerating voltage of 30 kV and beam currents 2.5 nA–80 pA. In the final step FIB operated at 1 kV/100 pA was used for 1 min on each side of the lamella, enabling the removal of the amorphous residue and gallium artefacts and reaching the desired thickness of < 20 nm, enabling atomic resolution in STEM.

High-resolution STEM experiments were performed on a probe Cs-corrected JEOL ARM 200 CF operated at 200 keV. The probe semi convergence angle was 24 mrad and the HAADF detection angles were set to 68–185 mrad. For chemical analysis Jeol Centurio EDX system with 100 mm2 SDD detector and Gatan Quantum ER double EELS spectrometer were used.

2.3. Atom probe tomography (APT)

Atom probe tomography (APT) specimens were prepared using the FIB-SEM lift-out process as described by Felfer et al. 2012 [14]. The two samples were run on local electrode atom probes (LEAP) 5000 series. The CHT specimen were run on a LEAP5000 XS at a base temperature of 60 K, a laser pulse energy of 60 pJ, with a pulse rate of 200 kHz and the detection rate set to 1 %. The DCT specimen were run on a LEAP5000 XR, at a base temperature of 60 K, a laser pulse energy of 60 pJ, a pulse rate of 200 kHz and a detection rate of 0.5 %. Data reconstruction and analysis were performed using AP Suite 6.3.

2.4. Scanning photoelectron microscopy (SPEM)

Scanning photoelectron microscopy (SPEM) was performed on the ESCA microscopy beamline at the Elettra Synchrotron Radiation Centre; more information about the technique can be found in [15–17].The base pressure of the microscope chamber was 3×10–10 mbar and the photon energy was 740 eV. Samples were pre-hardened and then analysed in-situ during CP (24 h) and tempering (823 K for 2 h for both samples) for both setups (CHT/CP). Prior to the experiments, the samples were ion sputtered with Ar to remove the oxide layer and surface contaminants. The cleanliness of each sample was thoroughly checked and no contaminants were found. The surface chemistry of the samples was mapped with high spatial resolution and spectral surveys. The surface chemical maps of C1s, Cr2p, Fe3p, Mn3p and V2p) were recorded at photon energies of 740 eV. For correct interpretation of the maps, a subtraction of the topography signal was also analysed using existing

procedures [18], so that the photoemission intensity maps represented the correct chemical contrast. Data analysis was performed using IgorPro9, WaveMetrics (Portland, OR, USA) and Origin, version 2022, OriginLab Corporation (Northampton, MA, USA).

3. Results and discussion

3.1. Alloy characterisation: microstructure and phase evolution

In this work, the high-Cr RAFM alloy, Eurofer, was subjected to conventional heat treatment procedure and additionally to CP (in-situ and ex-situ) in order to modify the dimensional stability and to saturate the matrix with carbides [19–21]. Microstructural changes were observed by scanning electron microscopy (SEM), transmission electron microscopy (TEM), energy dispersive X-ray analysis (EDX), electron backscatter diffraction (EBSD), atom probe tomography (APT) and X-ray diffraction (XRD). The results show that all three groups of samples (C-EF (control), T-EF (ex-situ CP) and ST-EF (in-situ CP)) have martensitic matrix embedded with different types of precipitates (carbides and carbonitrides). The distinct difference between the samples is induced by cryogenic processing, which on the one hand minimised the presence of retained austenite (RA) within the matrix by 75 % (T-EF) and 67 % (ST-EF), respectively (Fig. 1, Table 2). Furthermore, CP has influences also on the micrometre-sized martensitic laths, which are 30–40 % finer compared to those in C-EF and have a preferential orientation along [1 0 1] direction, whereas the C-EF counterpart doesn't have a preferential orientation. The change of orientation after CP correlates with previous findings for high Cr-alloys and martensitic stainless steels observed by Jovičević-Klug et al. 2021 [20] and Jovičević-Klug et al. 2023 [16]. On the other hand, cryogenic processing manipulated the precipitation of carbides (MxCy) and carbonitrides (MxCyNz) within the samples, increasing the volumetric fraction of the following precipitates: M_7C_3 by 15 % (T-EF), M_3C_2 by 21 %(ST-EF), $M_{23}C_6$ by 60 % for T-EF and 30 % for ST-EF, TaC by 66 % (T-EF) and 33 % (ST-EF) in compared to the C-EF. Observation also showed less precipitation or no change in precipitation in the tested samples (M_3C_2 and M_6C carbide types accordingly). The phenomenon originates from the different dynamics in the tested samples, which is induced by CP. This is an important observation as this can potentially influence the alloying dynamics and the formation of the passive film in terms of oxidation and its states within the samples.

Next observation also showed the presence of MCN and Ce-oxides (Supplementary Information–Fig. S1), whose presence is highly variable due to local distribution within each sample. The observed Ce-oxides (e.g. < 2 vol%) do not play an important microstructural role related to the precipitation dynamics. In addition, the TaC are not affected by the CP either, as their size and abundance remain unchanged. Fig. 1d shows the ratio of the precipitates within each sample, which indicates the precipitation dynamics induced by CP. Due to the changes in the nature of the carbides, the chemical composition has to be modified to compensate for the changes in the nucleation and growth of the carbides. EDX analysis of the carbides can identify these changes. The analysis confirms that primarily M_7C_3 carbides are enriched with Cr and Fe, M_6C are also enriched with Cr and Fe, whereas M_3C_2 are enriched with Cr, Fe and V. EDX analysis also confirms MCN precipitates, which are enriched in V (Fig. 2c–m).

Table 2
XRD results in volumetric fraction for all three samples, C-EF (control group), and testing groups ST-EF and T-EF:

	C-EF	T-EF	ST-EF
BCC phase	88.4	88.6	88.8
FCC phase	1.2	0.1	0.7
M_7C_3	3.5	4	3.4
M_3C_2	1.9	1.7	2.3
M_6C	1.7	1.1	1
$M_{23}C_6$	1	1.6	1.3
TaC	0.3	0.5	0.4
MCN	0.6	0.6	0.6
different Ce-oxides	1.4	1.8	1.5

However, based on SEM and EBSD results, no correlation in the distribution of carbides or carbonitrides can be correlated with CP, which contradicts the observation of many authors [16,21,22] in relation to CP in high Cr-alloys. No $M_{23}C_6$ carbides were detected at the microscopic level, which is different to previous studies [23,24]. However, EDX does not provide clear information on carbides below 100 nm, which are present in all samples, this was later obtained by TEM and APT. Due to the higher phase difference after CP, the T-EF was selected together with its counterpart, the C-EF, for detailed analysis with (S) TEM and APT (Fig. 2 and Fig. 3).

3.2. Nanoscale alloy characterization

TEM investigation of both samples confirms the presence of martensite within the matrix, C-EF in Fig. 3c–e and T-EF in Fig. 4c–e. RA was not detected due to the scarce spatial distribution as seen from EBSD results. Different types of carbides were identified in the vicinity of PAGs and newly formed GBs within the PAG (see Fig. 3g–h and Fig. 4g–h). The

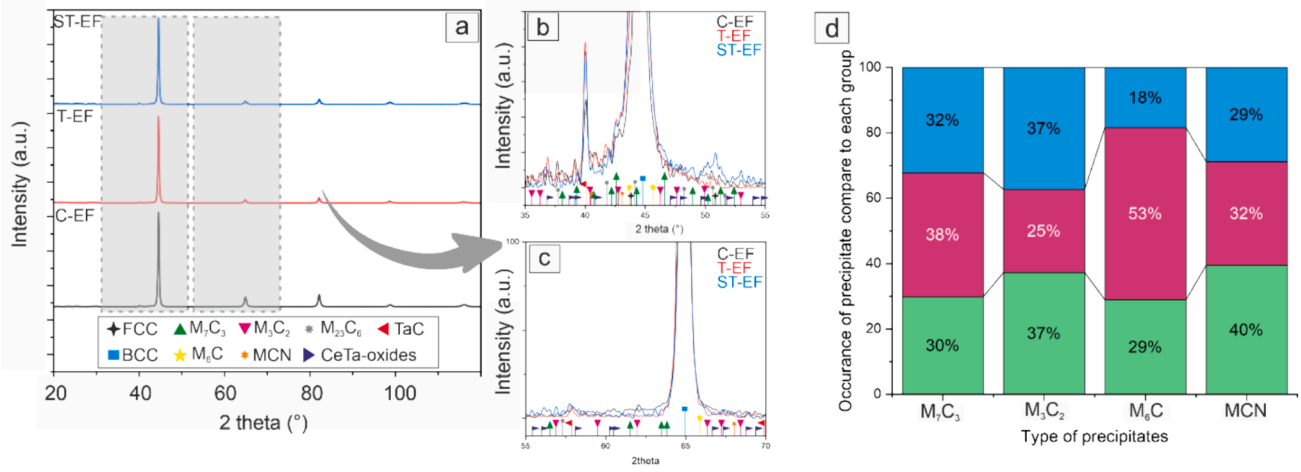

Fig. 1. A) xrd results for all 3 groups (c-ef (control), t-ef (ex-situ) and st-ef (in situ)) with corresponding main peak list displayed in the reference tab below. b) enlarged section of the xrd data from a) in the region of α-fe {1 1 0} peak. c) Enlarged section of the XRD data from a) in the region of α-Fe {2 0 1} peak. d) Graphically presented ratio of different precipitates within each sample extracted from the quantitative analysis of the XRD data. Blue colour stands for ST-EF, magenta for T-EF and green for C-EF sample.

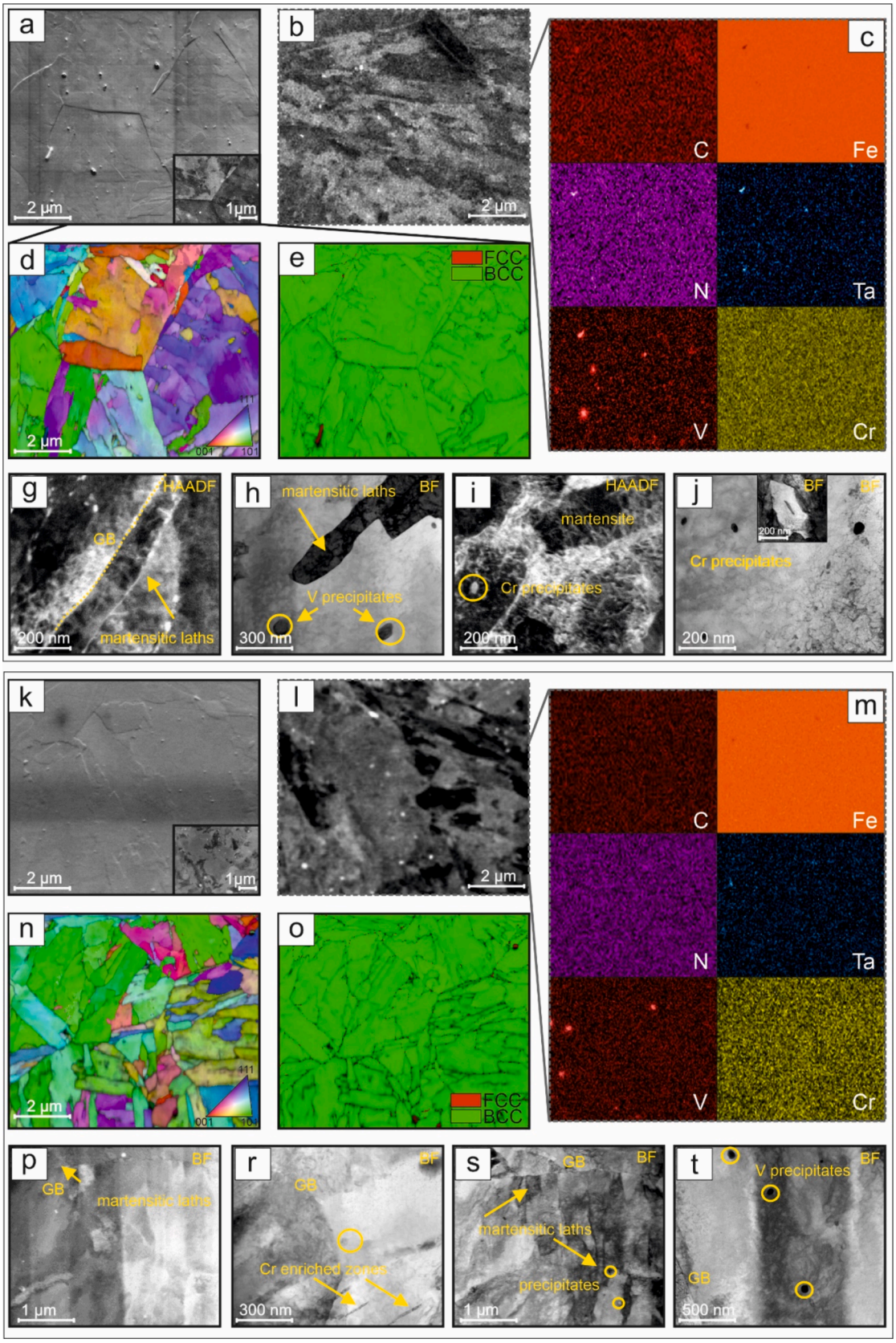

Fig. 2. The figure represents the results of SEM, EDX, EBSD and TEM (including HAADF and BF) results for selected samples of C-EF (a-j) and T-EF (k-t). Micrographs a, b and k, l present SEM micrographs obtained with SEI mode. Micrographs c and m present chemical distribution maps measured from areas presented in b and l, respectively. d and n present EBSD maps, while e and o present phase distribution maps. The analysed area from d, e and n, o correlate with the area from a and k, respectively. Micrographs g-j and p-t represent TEM (including HAADF and BF) images. The SEM and TEM analysis were performed on different sampling positions.

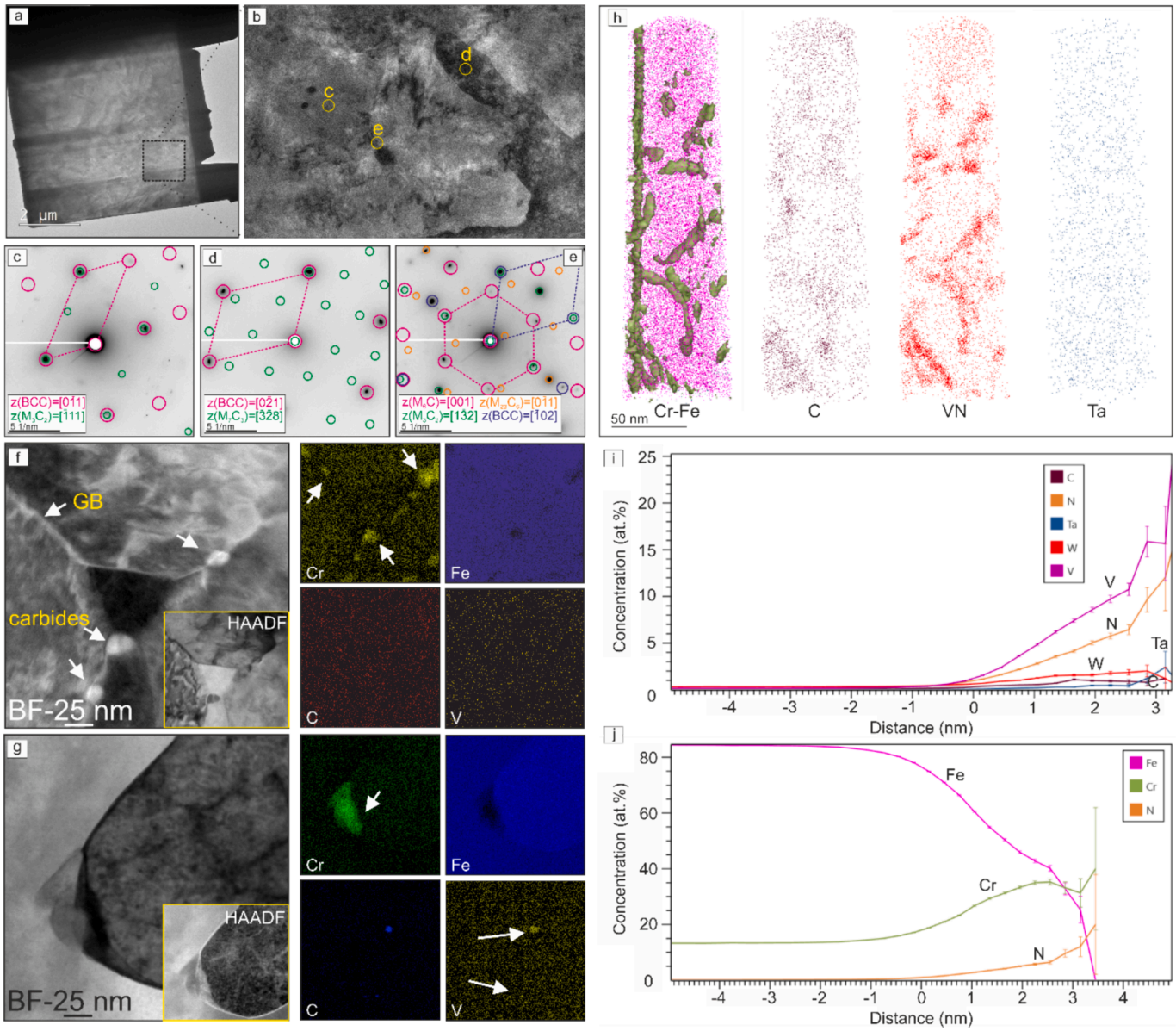

Fig. 3. a-b represent TEM micrographs of C-EF (control sample), where locations of SAED patterns are marked with yellow dots from c-e. STEM results for C-EF sample are presented in f-g parts (2 locations), where main elements such as Cr, Fe, C and V are presented. They were chosen based on important role, which they have in forming different types of precipitates. In h-i-j the results of APT analysis are presented. Part h represent 3D model with isosurface of Cr together with Fe, C, VN and Ta. I and j part represent proxigrams of selected carbide within the sample.

types, which were also confirmed with TEM and SAED on nanoscale are $(Fe, Cr)_3C_2$, $(Fe, Cr)_7C_3$ and (V, Ta)CN (Fig. 4). Furthermore, TEM has also confirmed the presence of $M_{23}C_6$ carbides corroborating with XRD results, which are enriched with Fe, Cr and Ta (Fig. 4e). There are two types of $M_{23}C_6$, one group holds larger (range of 100 nm) and is mostly enriched with Fe, Cr and Ta, whereas smaller fine carbides (in the range of 10 nm) are mostly enriched with Fe and Cr. These sub-micrometre carbides could indicate the slow transition of this type of $M_{23}C_6$ to M_6C carbides, which is the final carbide type after prolonged tempering [16,19].

In addition, Cr enrichment zones are found throughout the material that decorate the GBs (see example in Fig. 3g and h) and GBs intersections that in individual cases formed into larger agglomerates of Cr that are not in the form of carbides or nitrides as visible in Fig. 4g and h. A possible reasoning for these phases could be that they correspond to σ-phase of the Fe-Cr diagram that has the tendency to precipitate with austenite destabilization at PAG boundaries [25,26]. This also follows the probability that intermetallic phases, such as σ and χ phases, can form with prolonged exposure of Eurofer steel to temperatures of 550 °C and above [27]. A presence of conjoined V-rich carbide and Cr enrichment zone was observed with local EDX with TEM, as presented in the upper-right corner of Fig. 3g. The TEM results do not detect any dissimilarities between the T-EF and C-EF samples in terms of the Cr-rich phases. APT results identify rod-like precipitation of chromium vanadium nitrides within the C-EF sample, Fig. 3h. Trace amounts of C are also observed within these nitrides; however, the concentration is generally less than one atomic percent. Contrastingly both large and small chromium carbides are observed in the T-EF sample, Fig. 4h. Analysis of the concentration of both big and small precipitates indicates that Cr3C carbides have formed. The matrix composition for both C-EF and T-EF samples is approximately Fe 85 at.% and Cr 14 at.% with trace amounts of V, N, Mn, W, and C. APT also dislocate a slight Cr-enrichment forming around the precipitates as seen from Fig. 3j and 4j. The trend of Cr increase at the interface between matrix and carbides

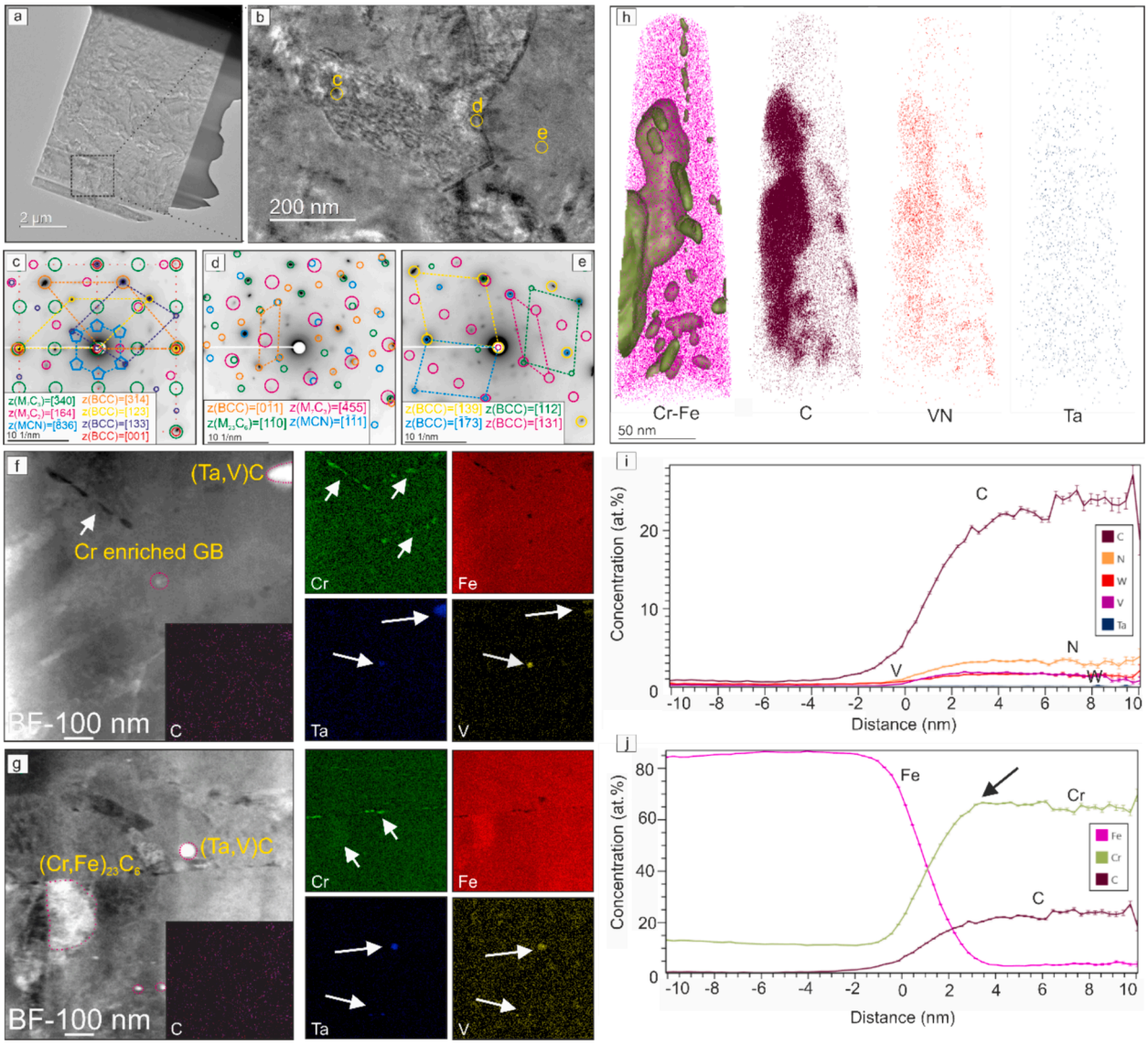

Fig. 4. a-b represent TEM micrographs of T-EF (tested sample), where locations of SAED patterns are marked with yellow dots from c-e. STEM results for C-EF sample are presented in f-g parts, where main elements such as Cr, Fe, C and V are presented. They were chosen based on important role, which they have in forming different types of precipitates. In h-i-j the results of APT analysis are presented. Part h represent 3D model with isosurface of Cr together with Fe, C, VN and Ta. I and j part represent proxigrams of selected carbide within the sample.

is also uncorrelated with C and N, which further corroborates to a possible Cr-enriched surface of the precipitates. In terms of size effect, the above-described features remain similar as seen from the additional analysis of smaller-size precipitates of the T-EF sample (Supplementary Information–Fig. S2).

The SAED confirms the presence of carbon-rich zones arranged in a hexagonal manner attributed to the $M_{23}C_6$ carbides. However, in specific instances of the T-EF sample, the enrichment zones display non-characteristic d-spacing that of $M_{23}C_6$ and are more likely to be related to the displacement of matrix phase interstitials in a specific low-symmetry quasi-structure. Individually, the SAED peaks could be partially related to a highly displaced M_7C_3 carbide form due to the superposition of the individual peaks and unique orientation with the zone axis (see example in Fig. 3d). Similar results were observed by Jovičević-Klug et al. for austenitic [28] and martensitic [20] stainless steels. This provides a reasoning to expect that after a short-time tempering at 550 °C the $M_{23}C_6$ carbides do in-fact evolve from the M_7C_3 through carbon diffusion and agglomeration at Cr-rich interfaces. The V-rich carbides are most probably residual structures that form from the austenitisation portion of the heat treatment and later act as heterogenous nucleation points for the carbides, similar as that of the Ta-rich particles. This also explains the highly varying and site-specific content of V, Ta and N in the precipitates that originates from the stochastic residual presence of the V- and Ta-enriched particles. The results provide a clear understanding of the initiation of further carbide development through the formation of additional GBs and interfaces that can hold greater amounts of carbon for CP samples. This can be seen by the obvious difference in the matrix density in terms of the number of martensitic laths forming within specific areas. As has been observed microscopically with SEM, TEM also confirms the much higher density of smaller-sized martensitic grains. This is best visualized by the staggering increase in the amount of the matrix peaks with varying orientations for the T-EF case compared to the C-EF case (compare Fig. 3c–e with Fig. 4c–e).

As a result, the increased density of GBs does accommodate an increased density of the carbides and intermetallic phases as their presence is detected in all boundaries. However, the thickness and size of the particles is lower compared to those found at the PAG boundaries,

which correlates well with the nucleation effect of residual V-rich and Ta-rich particles that also strongly decorate the PAG compared to the newly formed martensitic GBs. Additionally, insufficient chromium dissolvement and residual Cr enrichment at GBs can also Supplementary add to the increased nucleation at PAG boundaries. Surprisingly, the alloying content of the matrix for both samples is essentially the same (see APT results in Figs. 3 and 4), suggesting that the alloying of martensitic GBs occurs through GB diffusion rather than volumetric diffusion and most probably occurs during tempering as the martensitic lath density is influenced by the CP procedure [29,30].

3.3. Chemical binding state changes: In-situ observations

The SPEM technique was used to observe the in-situ and ex-situ behaviour of the selected alloying elements and their dynamics during formation of precipitates. The ex-situ experiments showed the carbide evolution of the proposed $M_{23}C_6$ carbides in both samples C-EF and T-EF (Fig. 5a, b, e and f). The maps suggest that after the application of CP, finer $M_{23}C_6$ carbides are formed, compared to C-EF sample, where already the nucleus from the pre-tempered state shows the location and growth of the carbide after tempering. They can be recognised by the specific content of Cr and Fe. $M_{23}C_6$ carbides in C-EF are larger and have a higher element content, while in T-EF they are much smaller and can hardly be detected, as their size is close to the system's spatial resolution. This observation also additionally confirms that carbides in both samples are not only located at the PAG positions but also within martensitic laths, which is best seen in Fig. 5e and f.

The single point analysis in spectra Fig. 5c, present the chemical changes on the location of the proposed larger $M_{23}C_6$ carbide (location indicated by star) before and after tempering in C-EF sample. The major difference is in the binding state of C1s, which is after tempering shifted towards lower values, which indicates a binding state change of the carbides after tempering (around 284 eV to 283–280.5 eV). In T-EF sample (Fig. 5g) chemical shift of carbon specific to fine $M_{23}C_6$ can be observed. Additionally, at 287 eV, the peak of C1s associated with binding state of carbonitrides (CN) can be observed for both C-EF (Fig. 5c) and T-EF (Fig. 5g) [31]. The C1s binding state indicate also different types of carbides on the same probed location, with the specific peak at approximately 280.5–281.5 eV corresponding most probably to complex Ta enriched carbide/carbonitride [31]. These features also confirm the proposed complex structure of individual carbides in agglomerates manner.

The correlation of the carbon shift is associated with the local chemistry contributed by the small-sized carbides visible from Fig. 5e and f as well as the similar shift seen from previous research [16,17]. Despite their smaller size, the single point SPEM analysis can be used to examine the chemical differences in the formed nanoscopic $M_{23}C_6$ carbides before (after CP) and after tempering. The spectra of $M_{23}C_6$ carbides reveal that their evolution is towards M6C composition (see Fig. 5h), which is similar to the observation done by Jovičević-Klug et al. 2023 for high-alloyed ferrous alloy (HAFA). In this case, additionally to Mo, W and low presence of V, an important role is played by Cr and to some degree also Fe (Fig. 5g). Furthermore, observation of C binding state change is also in line with the theory that loosely bound C is independent of the chemical composition of the matrix and non-stochiometric carbides, which are a chemically indifferent environment for the internal level of C, which was suggested by Gusev et al. 2001 [32].

It should be noted that these results show that also in Eurofer, W and Fe elemental ratio seems to slightly change, when individual carbides are formed with tempering, which corresponds to the carbide formation contribution of both elements, as determined by other research of HAFA [19,28]. Additionally, to conventionally expected alloying elements, Mn also participates in the formation of carbides, as seen from the Mn signal increase in Fig. 5d and h, similar as observed for HAFAs [17]. This change is observed for both samples, which can impact on the conductivity of the material [33]. The latter can be an important factor when dealing with electro-magnetic properties of Eurofer and its applications.

Ex-situ observation of both samples in regards to *O2s* and *Ta4f* have similar behaviour without any special dynamics, compared to other elements. An interesting specific is also the slightly higher intensity of *Fe3p* peak compared to the *Cr3p* peak for the T-EF compared to the C-EF (more measurements on different positions were performed and displayed same tendency), which suggest that most probably the formed carbides in the T-EF samples are on average smaller compared to those in C-EF sample as the additional matrix is probed more often. This could be possibly related to the refinement process and reduced nucleation energy of carbides precipitation with additional CP as determined from previous research [16,17,19,34].

In both samples in-situ observations showed that high Cr content plays an important role during formation of carbides, especially after CP and during tempering. In C-EF sample (sample with no CP, Fig. 5d) shows that in the final state the *Cr3p* peak is considerably stronger. This is suggested to be indicator of the development to M_7C_3 carbides as the final state [35]. Whereas in-situ observation of CP (T-EF sample, Fig. 6) showed that directly after CP the *Cr3p* is proportionally lower, which is associated to the diluted state of the matrix [35], and is associated to the increased formation of $M_{23}C_6$ carbides and later M_7C_3 carbides, as the final stable state, in alloy exposed to CP. This observation of the final development of the carbides in HAFA was also proposed as the main mechanism of CP by Jovičević-Klug et al. 2020 [19]. The presence of the slight shoulder/broadening of the C1s peak, seen in Fig. 6d, towards lower values furthermore supports the reforming of the binding state of Cr with CP. In-situ observation of *Ta4f* has shown that Ta is more in a metal state after tempering, since it is shifted more to the structure of more complex Ta carbides [36], which indicate the partial role in $M_{23}C_6$ carbide formation [37]. Furthermore, due to the broadening of the *O2s* + *Ta4f* peak, it is suggested that Ta is partially present in an oxide form, which suggest that Ta plays also a role in oxide layer at the surface of the Eurofer, that is related to passivation layer build-up. The slight build-up of upper oxide layer that inevitably forms in investigated samples over time, provides direct evidence of Ta and Cr enrichment (see colour change and contrast increase in Fig. 5e–f and 6a–b, indicating that both elements are key participations in the oxidation of the alloy and its surface. Similar suggestion was done also by Ström et al. 2018 [38], however this observation was done after exposure to deuterium ion beam and high temperatures.

4. Conclusions

In this work, we have found that the processing history of a high-Cr ferrous alloy (Eurofer) is very important in terms of manipulating the microstructure and hence the precipitation of the selected carbides. As the literature conveys, prolonged exposure of Eurofer to extreme conditions increases carbide precipitation and with it modifies the dimensional stability of the alloy, which can lead to material failure. With this study we present that CP can be used to successfully manipulate the microstructure by increasing precipitation of nanoprecipitates, which are mainly $M_{23}C_6$. The resulting microstructure develops a deficit of free atoms of alloying elements, which is suggested to lower the possibility of later microstructure deterioration and modification under extreme fusion conditions. Furthermore, the performed in-situ and ex-situ measurements provided an in-detail investigation of the dynamics of alloying elements during CP and their role in the formation of precipitates after CP and after tempering. The study also shows that the Ta dynamics on the surface layer may be important for the characteristics of the passivation layer, which plays an important role in the corrosion, oxidation, and wear resistance of Eurofer.

It should be noted that our study has not yet tested the newly tailored microstructure of CP under irradiation or other corrosive or wear properties, which will provide direct evidence for a CP effect on Eurofer

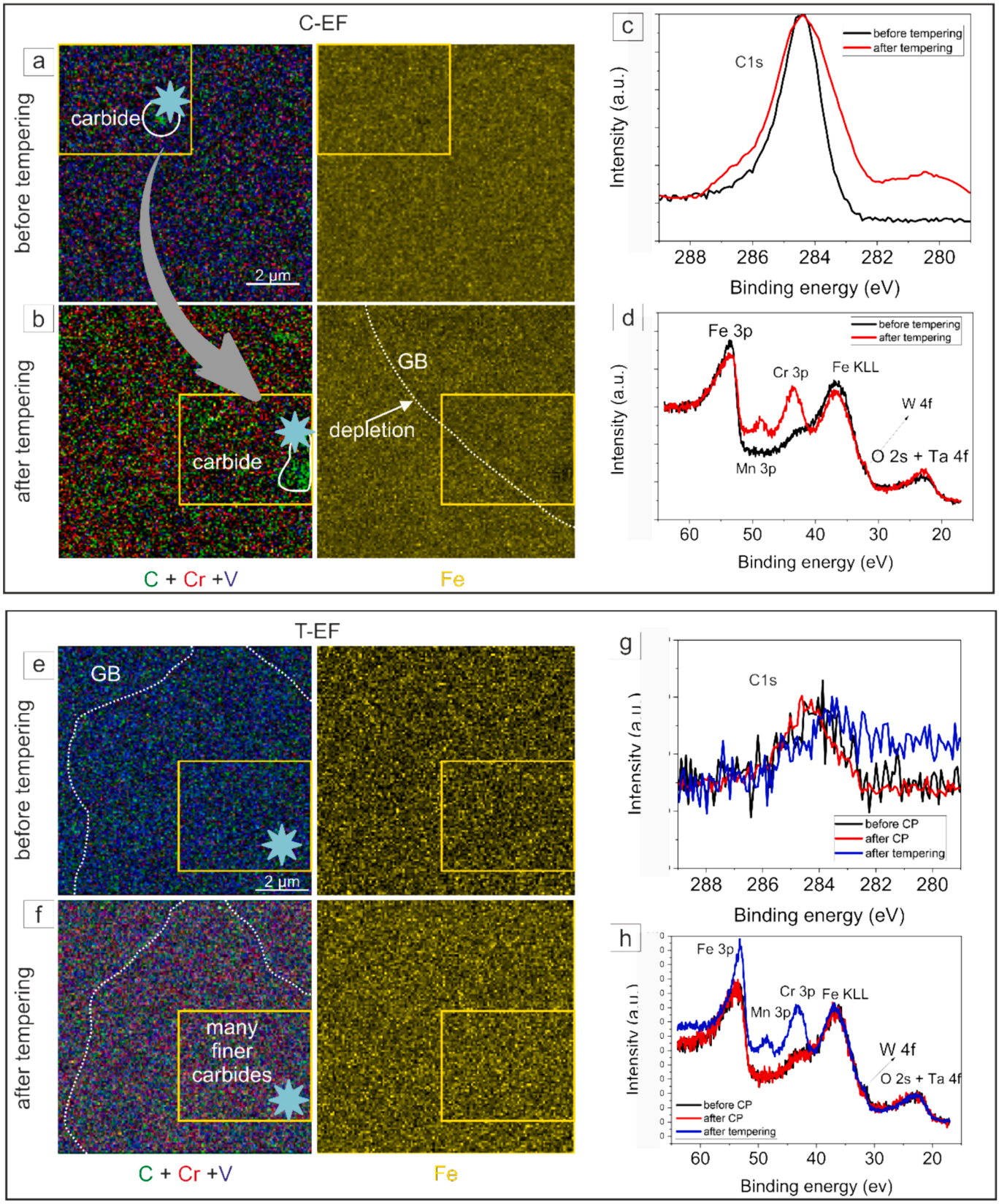

Fig. 5. represents the results of SPEM ex-situ measurements of C-EF (a-d) and T-EF sample (e-h). For both samples mapping of selected alloying elements such as C, Cr, V and Fe was performed in order to identify their role in the formation of carbides (a-b and e-f). Whereas c-d and g-h graphs represent point spectra analysis of C1s (c,g) and Fe3p, Mn3p, Cr3p, W4f and O2s + Ta 4f.

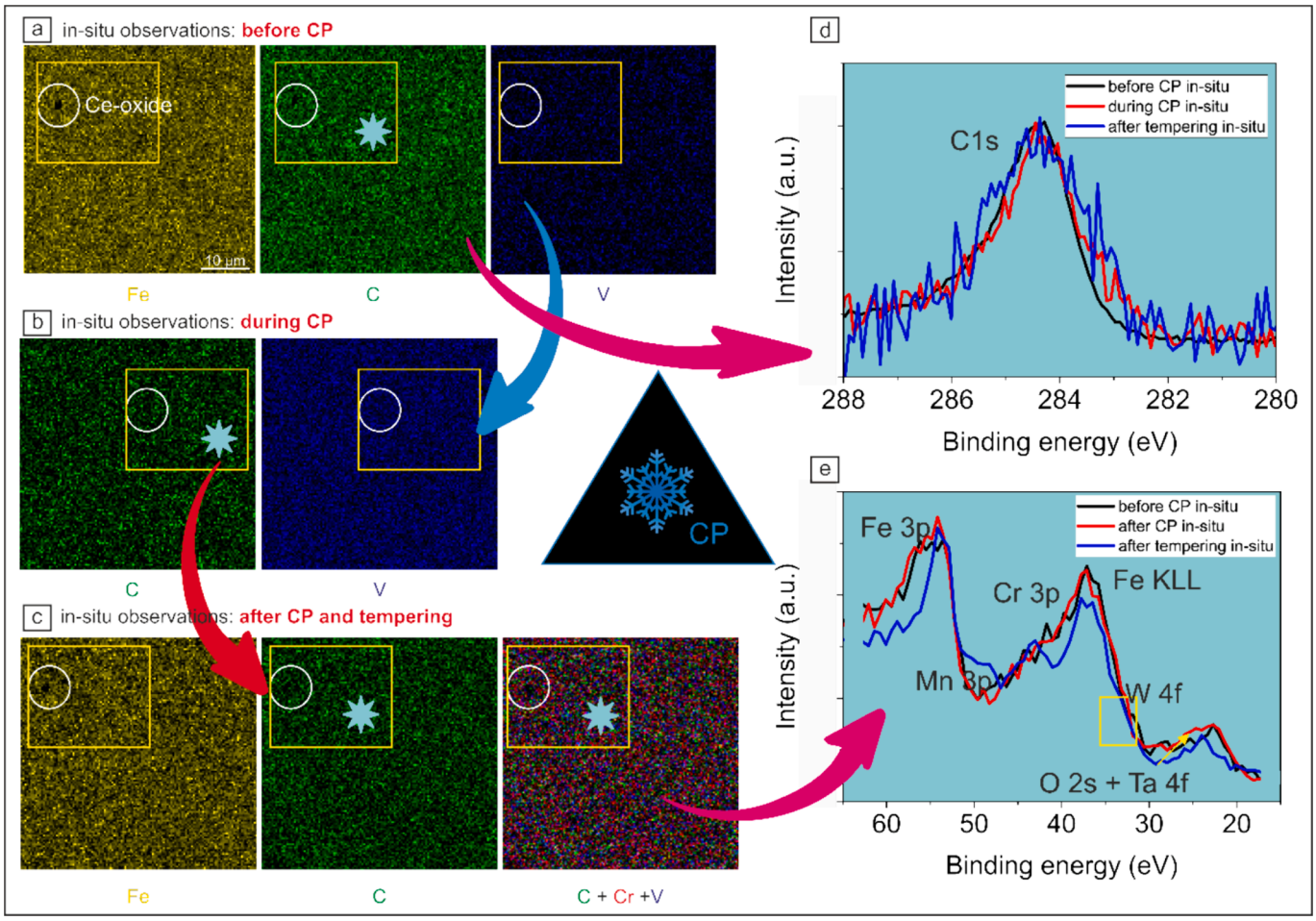

Fig. 6. represents in-situ observation of T-EF sample, before CP, directly after CP and after tempering, so that effect of CP on the sample can be observed. a-c mapping shows in-situ observations of selected alloying elements.

stability. However, this microstructure study provides guidance for the selection of the best processing route for Eurofer and provides insight into possible progression of carbide formation with CP. The aim of this work was also achieved in providing fundamental understanding of the alloying elements and their effect on the surface oxide layer after the application of CP. This study also shows that CP has a bright future in alloying metallic alloys and to design a proper heat processing for changing properties for community to accelerate the understanding of Eurofer alloying dynamic and how the microstructure can be tailored to specific needs and applications.

CRediT authorship contribution statement

Patricia Jovičević-Klug: Writing – review & editing, Writing – original draft, Validation, Methodology, Investigation, Formal analysis. **Carsten Bonnekoh:** Writing – review & editing, Writing – original draft, Resources, Methodology, Conceptualization. **Matic Jovičević-Klug:** Writing – review & editing, Writing – original draft, Validation, Methodology, Investigation, Formal analysis. **Bojan Ambrožič:** Writing – review & editing, Writing – original draft, Methodology. **Goran Dražić:** Writing – review & editing, Writing – original draft, Methodology. **Zygmunt Miłosz:** Writing – review & editing, Writing – original draft, Methodology. **Yan Ma:** Writing – review & editing, Writing – original draft, Methodology. **Ingrid McCarroll:** Writing – review & editing, Writing – original draft, Methodology. **Benjamin Breitbach:** Writing – review & editing, Writing – original draft, Methodology. **Matteo Amati:** Writing – review & editing, Writing – original draft, Supervision, Methodology. **Luca Gregoratti:** Writing – review & editing, Writing – original draft, Supervision, Methodology. **Michael Rieth:** Writing – review & editing, Supervision, Resources. **Michael Rohwerder:** Writing – review & editing, Supervision, Resources.

Declaration of competing interest

The authors declare that they have no known competing financial interests or personal relationships that could have appeared to influence the work reported in this paper.

Data availability

Data will be made available on request.

This study was mainly funded by Alexander von Humboldt Foundation PostDoc Fellowship, which recipient was Dr Patricia Jovičević-Klug. Dr. Patricia Jovičević-Klug acknowledge Elettra Sincrotrone Trieste for providing access to its synchrotron radiation facilities and for financial support under the IUS internal project. The travel costs and accommodation were also supported by 20230078 proposal grant, which recipient was Dr: Patricia Jovičević-Klug. Accommodation and travel costs for research stay at Basovizza was covered by grant 2023-23099 provided by Zavod ABIONA for Dr. Matic Jovičević-Klug.

Appendix A. Supplementary data

Supplementary data to this article can be found online at https://doi.org/10.1016/j.apsusc.2024.160290.

References

[1] M. Shahwaz, P. Nath, I. Sen, A critical review on the microstructure and mechanical properties correlation of additively manufactured nickel-based superalloys, J Alloys Compd 907 (2022) 164530, https://doi.org/10.1016/J.JALLCOM.2022.164530.

[2] P. Jovičević-Klug, M. Rohwerder, Sustainable New Technology for the Improvement of Metallic Materials for Future Energy Applications, Coatings 2023, Vol. 13, Page 1822 13 (2023) 1822. DOI: 10.3390/COATINGS13111822.

[3] T. Kletz, P. Amyotte, What Went Wrong?: case Histories of Process Plant Disasters and How They Could Have Been Avoided, Elsevier, BH, Oxford, UK, 2019.

[4] G.S. Was, D. Petti, S. Ukai, S. Zinkle, Materials for future nuclear energy systems, J. Nucl. Mater. 527 (2019) 151837, https://doi.org/10.1016/J.JNUCMAT.2019.151837.

[5] K.D. Zilnyk, H.R.Z. Sandim, R.E. Bolmaro, R. Lindau, A. Möslang, A. Kostka, D. Raabe, Long-term microstructural stability of oxide-dispersion strengthened Eurofer steel annealed at 800 °C, J. Nucl. Mater. 448 (2014) 33–42, https://doi.org/10.1016/J.JNUCMAT.2014.01.032.

[6] K.D. Zilnyk, P.A. Suzuki, H.R.Z. Sandim, Subtle microstructural changes during prolonged annealing of ODS-Eurofer steel, Nucl. Mater. Energy 35 (2023) 101450, https://doi.org/10.1016/J.NME.2023.101450.

[7] X. Chen, A. Bhattacharya, M.A. Sokolov, L.N. Clowers, Y. Yamamoto, T. Graening, K.D. Linton, Y. Katoh, M. Rieth, Mechanical properties and microstructure characterization of Eurofer97 steel variants in EUROfusion program, Fusion Eng. Des. 146 (2019) 2227–2232, https://doi.org/10.1016/J.FUSENGDES.2019.03.158.

[8] C. Cabet, F. Dalle, E. Gaganidze, J. Henry, H. Tanigawa, Ferritic-martensitic steels for fission and fusion applications, J. Nucl. Mater. 523 (2019) 510–537, https://doi.org/10.1016/J.JNUCMAT.2019.05.058.

[9] A. Zakirov, Influence of the Bulk Chemical Composition on the Microstructure Evolution of Irradiated Chemically-tailored Nuclear RPV Steels, (2022). https://theses.hal.science/tel-04025831 (accessed December 7, 2023).

[10] Z. Shen, D. Tweddle, H. Yu, G. He, A. Varambhia, P. Karamched, F. Hofmann, A. J. Wilkinson, M.P. Moody, L. Zhang, S. Lozano-Perez, Microstructural understanding of the oxidation of an austenitic stainless steel in high-temperature steam through advanced characterization, Acta Mater 194 (2020) 321–336, https://doi.org/10.1016/J.ACTAMAT.2020.05.010.

[11] B. Zhu, Y. Wang, J. Dluhoš, A.J. London, M. Gorley, M.J. Whiting, T. Sui, A novel pathway for multiscale high-resolution time-resolved residual stress evaluation of laser-welded Eurofer97, Sci Adv 8 (2022) 4592. DOI: 10.1126/SCIADV.ABL4592/ASSET/F0837818-4E97-49EB-908C-E8A3E07D4A61/ASSETS/IMAGES/LARGE/SCIADV.ABL4592-F5.JPG.

[12] E. Materna-Morris, C. Adelhelm, S. Baumgärtner, B. Dafferner, P. Graf, S. Heger, U. Jäntsch, R. Lindau, C. Petersen, M. Rieth, R. Ziegler, H. Zimmermann, F. Karlsruhe, Final Report on the EFDA Task STRUCTURAL MATERIAL EUROFER97-2, Characterization of Rod and Plate Material: structural, Charpy, and Creep Properties, Tensile, 2007.

[13] P. Jovičević-Klug, N. Lipovšek, M. Jovičević-Klug, B. Podgornik, Optimized preparation of deep cryogenic treated steel and Al-alloy samples for optimal microstructure imaging results, Mater Today Commun 27 (2021) 102211, https://doi.org/10.1016/j.mtcomm.2021.102211.

[14] P.J. Felfer, T. Alam, S.P. Ringer, J.M. Cairney, A reproducible method for damage-free site-specific preparation of atom probe tips from interfaces, Microsc Res Tech 75 (2012) 484–491, https://doi.org/10.1002/JEMT.21081.

[15] M.K. Abyaneh, L. Gregoratti, M. Amati, M. Dalmiglio, M. Kiskinova, Scanning photoelectron microscopy: a powerful technique for probing micro and nano-structures, e-J. Surf. Sci. Nanotechnol. 9 (2011) 158–162, https://doi.org/10.1380/EJSSNT.2011.158.

[16] P. Jovičević-Klug, L. Tegg, M. Jovičević-Klug, R. Parmar, M. Amati, L. Gregoratti, L. Almasy, J.M. Cairney, B. Podgornik, Understanding carbide evolution and surface chemistry during deep cryogenic treatment in high-alloyed ferrous alloy, Appl Surf Sci 610 (2023) 155497, https://doi.org/10.1016/j.apsusc.2022.155497.

[17] P. Jovičević-Klug, M. Jovičević-Klug, L. Tegg, D. Seidler, L. Thormahlen, R. Parmar, M. Amati, L. Gregoratti, J.M. Cairney, J. McCord, M. Rohwerder, B. Podgornik, Correlative surface and bulk analysis of deep cryogenic treatment influence on high-alloyed ferrous alloy, J. Mater. Res. Technol. 11–12 (2022) 4799–4810.

[18] L. Gregoratti, M. Marsi, G. Cautero, M. Kiskinova, G.R. Morrison, A.W. Potts, Spectromicroscopy of interfaces with synchrotron radiation: multichannel data acquisition, Nucl. Inst. Methods Phys. Res. A (2001) 884–888.

[19] P. Jovičević-Klug, M. Jovičević-Klug, B. Podgornik, Effectiveness of deep cryogenic treatment on carbide precipitation, J. Mater. Res. Technol. 9 (2020) 13014–13026, https://doi.org/10.1016/j.jmrt.2020.09.063.

[20] P. Jovičević-Klug, M. Jovičević-Klug, T. Sever, D. Feizpour, B. Podgornik, Impact of steel type, composition and heat treatment parameters on effectiveness of deep cryogenic treatment, J. Mater. Res. Technol. 14 (2021) 1007–1020.

[21] P. Jovičević-Klug, M. Jovičević-Klug, L. Thormählen, J. McCord, M. Rohwerder, M. Godec, B. Podgornik, Austenite reversion suppression with deep cryogenic treatment: a novel pathway towards 3rd generation advanced high-strength steels, Mater. Sci. Eng. A 873 (2023) 145033, https://doi.org/10.1016/J.MSEA.2023.145033.

[22] G. Prieto, J.E.P. Ipiña, W.R. Tuckart, Cryogenic treatments on AISI 420 stainless steel: microstructure and mechanical properties, Mater. Sci. Eng. A 605 (2014) 236–243, https://doi.org/10.1016/J.MSEA.2014.03.059.

[23] M. Duerrschnabel, U. Jäntsch, R. Gaisin, M. Rieth, Microstructural insights into EUROFER97 batch 3 steels, Nucl. Mater. Energy 35 (2023) 101445, https://doi.org/10.1016/J.NME.2023.101445.

[24] M. Klimenkov, U. Jäntsch, M. Rieth, A. Möslang, Correlation of microstructural and mechanical properties of neutron irradiated EUROFER97 steel, J. Nucl. Mater. 538 (2020) 152231, https://doi.org/10.1016/J.JNUCMAT.2020.152231.

[25] Y. Shen, X. Zhou, T. Shi, X. Huang, Z. Shang, W. Liu, B. Ji, Z. Xu, Sigma phases in an 11%Cr ferritic/martensitic steel with the normalized and tempered condition, Mater Charact 122 (2016) 113–123, https://doi.org/10.1016/J.MATCHAR.2016.10.031.

[26] M.H. Lewis, Precipitation of (Fe, Cr) sigma phase from austenite, Acta Metall. 14 (1966) 1421–1428, https://doi.org/10.1016/0001-6160(66)90162-3.

[27] M. Rieth, M. Dürrschnabel, S. Bonk, U. Jäntsch, T. Bergfeldt, J. Hoffmann, S. Antusch, E. Simondon, M. Klimenkov, C. Bonnekoh, B.E. Ghidersa, H. Neuberger, J. Rey, C. Zeile, G. Pintsuk, G. Aiello, Technological Processes for Steel Applications in Nuclear Fusion, Applied Sciences 2021, Vol. 11, Page 11653 11 (2021) 11653. DOI: 10.3390/APP112411653.

[28] P. Jovičević-Klug, N. Lipovšek, M. Jovičević-Klug, M. Mrak, J. Ekar, B. Ambrožič, G. Dražić, J. Kovač, B. Podgornik, Assessment of deep cryogenic heat-treatment impact on the microstructure and surface chemistry of austenitic stainless steel, Surf. Interfaces (2022) 102456, https://doi.org/10.1016/J.SURFIN.2022.102456.

[29] Z. Tokei, K. Hennesen, H. Viefhaus, H.J. Grabke, Diffusion of chromium in ferritic and austenitic 9–20 wt-%chromium steels, Mater. Sci. Technol. 16 (2000) 1129–1138, https://doi.org/10.1179/026708300101507055.

[30] M. Mizouchi, Y. Yamazaki, Y. Iijima, K. Arioka, Low Temperature Grain Boundary Diffusion of Chromium in SUS316 and 316L Stainless Steels, n.d.

[31] I. Kusunoki, M. Sakai, Y. Igari, S. Ishidzuka, T. Takami, T. Takaoka, M. Nishitani-Gamo, T. Ando, XPS study of nitridation of diamond and graphite with a nitrogen ion beam, Surf Sci 492 (2001) 315–328, https://doi.org/10.1016/S0039-6028(01)01430-3.

[32] A.I. Gusev, A.A. Rempel, A.J. Magerl, Disorder and Order in Strongly Nonstoichiometric Compounds, Springer, New York, NY, USA, 2001.

[33] S. Dang, Y. Wen, T. Qin, J. Hao, H. Li, J. Huang, D. Yan, G. Cao, S. Peng, Nanostructured manganese dioxide with adjustable Mn3+/Mn4+ ratio for flexible high-energy quasi-solid supercapacitors, Chem. Eng. J. 396 (2020) 125342, https://doi.org/10.1016/J.CEJ.2020.125342.

[34] P. Jovičević-Klug, A.Z. Guštin, M. Jovičević-Klug, B. Šetina Batič, A. Lebar, B. Podgornik, Coupled role of alloying and manufacturing on deep cryogenic treatment performance on high-alloyed ferrous alloys, J. Mater. Res. Technol. 18 (2022) 3184–3197, https://doi.org/10.1016/J.JMRT.2022.04.025.

[35] M. Detroye, F. Reniers, C. Buess-Herman, J. Vereecken, AES–XPS study of chromium carbides and chromium iron carbides, Appl Surf Sci 144–145 (1999) 78–82, https://doi.org/10.1016/S0169-4332(98)00769-7.

[36] S. Kumar, S. Mondal, A. Kumar, A. Ranjan, N.E. Prasad, Chemical Vapor Deposition of TaC/SiC on Graphite Tube and Its Ablation and Microstructure Studies, Coatings 2017, Vol. 7, Page 101 7 (2017) 101. DOI: 10.3390/COATINGS7070101.

[37] A. Nisar, T. Sakthivel, C. Zhang, B. Boesl, S. Seal, A. Agarwal, Quantification of complex protective surface oxide layer formed during plasma jet exposure of multicomponent ultra-high temperature carbides, Appl Surf Sci 592 (2022), https://doi.org/10.1016/J.APSUSC.2022.153247.

[38] P. Ström, P. Petersson, R. Arredondo Parra, M. Oberkofler, T. Schwarz-Selinger, D. Primetzhofer, Sputtering of polished EUROFER97 steel: surface structure modification and enrichment with tungsten and tantalum, J. Nucl. Mater. 508 (2018) 139–146, https://doi.org/10.1016/J.JNUCMAT.2018.05.031.